Reconstructing the neutrally-buoyant particle flow near a singular corner

Francesco Romanò*

[1] *Univ. Lille, CNRS, ONERA, Arts et Métiers Institute of Technology, Centrale Lille, UMR 9014 -LMFL - Laboratoire de Mécanique des Fluides de Lille - Kampé de Fériet, F-59000 Lille, France*

The correction of buoyancy effects is tackled for particles moving close to a singular corner in creeping flow conditions. A few density-mismatched particle trajectories are used to reconstruct the dynamics of a neutrally-buoyant particle all over the target domain. We propose to take advantage of the dissipative dynamics of density-mismatched particles in order to probe the target domain. Thereafter, we retrieve the neutrally-buoyant particle flow all over the domain by reconstructing the phase space of the density-mismatched particulate flow and taking the limit of the particle-to-fluid density ratio tending to one. The robustness of such an approach is demonstrated by deliberately ill-conditioning the reconstruction operator. In fact, we show that our algorithm well performs even when we rely on qualitatively-different density-mismatched orbit topologies or on bundles of close trajectories rather than homogeneously distributed orbits. Potential applications to microfluidics and improvements of the proposed algorithm are finally discussed.

Citation: F. Romanò, Reconstructing the neutrally-buoyant particle flow near a singular corner, Acta Mech. Sin. **38**, 721490 (2022), https://doi.org/10.1007/s10409-022-09025-x

1. Introduction

Particle-laden flows are multiphase flows for which the dispersed phase is made of rigid particles immersed in the carrier (fluid) phase. Their relevance to industrial applications (e.g., aerosol technology [1], or combustion [2]) and natural phenomena (e.g., transport of red blood cells [3], or debris flows [4]) remarks the ubiquity of particle suspensions, both in turbulent and laminar flows. Among the laminar flows, suspended particles are frequently used in small-scale systems such as in microfluidic [5,6] and lab-on-a-chip [7, 8] devices, or to deliver drugs [9, 10] and replace surfactant [11, 12]. As the typical velocity scales associated to micro- and nano-fluidic systems are slow, and the characteristic lengths scales are small, the Stokesian approximation of such flows is commonly employed.

To date, several modeling approaches have been proposed for particles in unbounded flows [13-15] and complementary exact [16, 17], numerical [18, 19], asymptotic [20-23], or modeled [24-26] corrections attempted to include particle-boundary interactions in the original equation of Maxey and Riley [13]. Despite the well established mathematical framework, understanding and predicting the dynamics of the particulate phase is still a challenge. In particular, the intrinsically dissipative dynamics of most of the forces exerted by the fluid on the particle may lead to the formation of intricate attractors either because of high-strain regions [27, 28], particle-boundary interactions [29-31], Coriolis [32, 33], or inertial [34-36] effects. The picture becomes even more complex when considering that a qualitatively novel dynamics can emerge when two or more of such effects gets combined. This is the case, for instance, of the non-trivial attactors reported for inertial particles in steady [37, 38] or oscillatory [39-41] cavity flows. The prediction of the particle dynamics becomes even more challenging when the particles are immersed in a complex chaotic fluid flow [42, 43], where non-

*Corresponding author. E-mail address: francesco.romano@ensam.eu (Francesco Romanò)

Executive Editor: Cristian Marchioli

dissipative forces, such as buoyancy, actively contribute to a symmetry breaking [44] or to the creation of attractors [45].

Starting from the method originally proposed by Romanò [46] for retrieving the velocity field in the tracer limit, this paper will extend our previous approach by demonstrating that a similar method has potential for targeting a different objective, i.e., predicting the dynamics of neutrally-buoyant finite-size particles. As in Ref. [46], we will still rely on the trajectories of a few large density-mismatched inertial particles, but contrary to Ref. [46] we will not take the tracer limit (Stokes number tending to zero). This will allow us to correct for sedimentation and density-mismatch effects, i.e., to reconstruct the dynamics of a neutrally-buoyant particle preserving the dissipative effects due to its finite size and to the corresponding interaction with the boundaries. The aim is to demonstrate that a robust reconstruction of the particulate phase space for the neutrally-buoyant particle is possible, even for singular flows as the one considered in this paper (not yet demonstrated by Ref. [46]). Such a correction for density-mismatch effect can help to better understand the particle dynamics in phase space, as a major source of dissipation can be corrected for. This will be demonstrated for a singular corner flow that reflects the Taylor's scraper problem [47]. The forces and torques on a sphere near the right dihedral corner in Stokes flow have been numerically computed by Ref. [48] and are here used to integrate the particle trajectories. At first, the mathematical problem is formulated in Sect. 2, then the particulate flow is defined by taking advantage of the symmetries of the problem and of the linearity of the creeping flow approximation (see Sect. 3). Thereafter, the technique proposed for the phase-space reconstruction is presented in Sect. 4 and the corresponding are analysed and discussed in Sect. 5. A summary, some conclusions and the future perspectives of our approach are finally reported in Sect. 6.

2. Problem formulation

The motion of a rigid sphere near a semi-infinite right dihedral corner made by two solid walls is considered. The spherical particle of density ρ_p and radius a_p moves with translational velocity $\tilde{\boldsymbol{U}} = (\tilde{U}, \tilde{V}, \tilde{W})$ and rotational velocity $\tilde{\boldsymbol{\Omega}} = (\tilde{\Omega}_x, \tilde{\Omega}_y, \tilde{\Omega}_z)$. The sphere is immersed in a Newtonian fluid of constant density ρ_f and kinematic viscosity ν. One of the two corner walls slides tangentially to its own plane at $z = 0$ with velocity $\tilde{\boldsymbol{U}}_\mathrm{w} = (\tilde{U}_\mathrm{w},\ 0,\ 0)$. By moving towards the corner edge located at $\tilde{\boldsymbol{x}} = (0, \tilde{y}, 0)$, the sliding wall drives an incompressible flow between the particle and the walls. Moreover, owing to the density mismatch, also the buoyancy force due to the gravitational acceleration $\boldsymbol{g} = g(0, 0, 1)$ contribute to establish the fluid flow (see Fig. 1).

The particle experiences a creeping flow if the local particle Reynolds number is small, i.e., $emphRe_\mathrm{p} = |\tilde{\boldsymbol{U}} + \tilde{\boldsymbol{\Omega}} \times \left(\tilde{\boldsymbol{x}}_\mathrm{s} - \tilde{\boldsymbol{x}}_\mathrm{p}\right) - \tilde{\boldsymbol{u}}|a_\mathrm{p}/\nu \ll 1$, where $\tilde{\boldsymbol{x}}_\mathrm{p} = (\tilde{x}_\mathrm{p}, \tilde{y}_\mathrm{p}, \tilde{z}_\mathrm{p})$ is the position vector of the particle centroid, while $\tilde{\boldsymbol{x}}_\mathrm{s}$ denotes the particle surface. Moreover, considering a region at distance L from the corner edge, also the near-corner flow driven by the sliding wall can be assumed Stokesian if $emphRe = |\tilde{U}_\mathrm{w}|L/\nu \ll 1$. When both such assumptions hold, the inertial term of the momentum equation can be neglected and the fluid flow between the particle and the corner is governed by the incom-

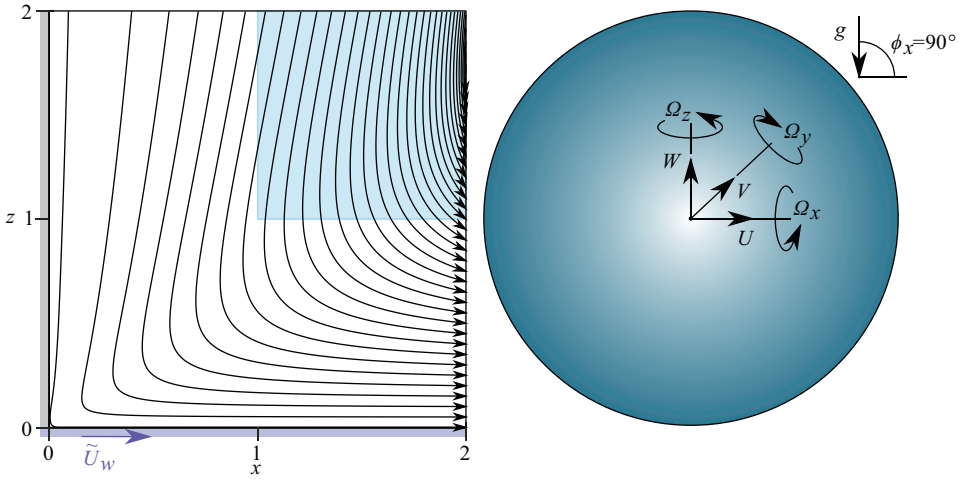

Figure 1 Spherical particle moving near a dihedral corner with a wall sliding at velocity $\tilde{\boldsymbol{U}}_\mathrm{w} = (\tilde{U}_\mathrm{w},\ 0,\ 0)$. The sphere is subject to the forces exerted by the surrounding fluid and by the gravitational acceleration $\boldsymbol{g}$. The solid lines represent the streamlines of the Stokes flow without the particle, and the light-blue region denotes the subdomain accessible to the particle centroid, considering that the sphere cannot penetrate the walls. The dynamics of the particle is therefore considered within the light-blue domain, whereas the fluid domain extension in x- and z- direction is of $360a_\mathrm{p}$, and of $720a_\mathrm{p}$ in y-direction (same domain as in Ref. [48]).

pressible creeping flow equations:

$$\nabla \cdot \boldsymbol{u} = 0, \qquad \nabla p = \nabla^2 \boldsymbol{u}, \tag{1}$$

where $\boldsymbol{u}$ is the dimensionless velocity field of the fluid phase and p its reduced pressure field. The non-dimensional form of the equations has been obtained by scaling lengths ($\tilde{\boldsymbol{x}}$, $\tilde{\boldsymbol{x}}_\mathrm{p}$, $\tilde{\boldsymbol{x}}_\mathrm{s}$), velocities ($\tilde{\boldsymbol{U}}$, $\tilde{\boldsymbol{U}}_\mathrm{w}$) and pressure ($\tilde{p}$) by a_p, ν/a_p and $\rho_\mathrm{f}\nu^2/a_\mathrm{p}^2$, respectively; consistently, the rotation rate of the particle ($\tilde{\boldsymbol{\Omega}}$) is scaled by ν/a_p^2. Below, the tilde-sign is dropped for denoting the non-dimensional quantities.

The mathematical problem (1) is closed by the no-slip boundary conditions at the solid walls and over the particle surface

$$x = 0: \quad \boldsymbol{u} = \boldsymbol{0}, \tag{2a}$$
$$z = 0: \quad \boldsymbol{u} = \boldsymbol{U}_\mathrm{w}, \tag{2b}$$
$$\boldsymbol{x} = \boldsymbol{x}_\mathrm{s}: \quad \boldsymbol{u} = \boldsymbol{U} + \boldsymbol{\Omega} \times (\boldsymbol{x}_\mathrm{s} - \boldsymbol{x}_\mathrm{p}), \tag{2c}$$

and by enforcing the far-field conditions for the fluid flow at a distance L/a_p from the corner edge. For $|\boldsymbol{x}_\mathrm{p}| \ll L/a_\mathrm{p}$ we can safely assume that the particle perturbation has vanished (see Romanò et al. [48]), hence the far-field flow is enforced to correspond to the analytical solution of the Taylor's scraper flow [47], i.e.,

$$u = U_\mathrm{w}\left[f'(\theta)\cos(\theta) + f(\theta)\sin(\theta)\right], \tag{3a}$$
$$v = 0, \tag{3b}$$
$$w = U_\mathrm{w}\left[f'(\theta)\sin(\theta) - f(\theta)\cos(\theta)\right], \tag{3c}$$

where $\theta = \cos^{-1}\left(x/\sqrt{x^2+z^2}\right)$ is the polar angle and $f(\theta) = [\theta\sin(\pi/2-\theta) - \pi/2(\pi/2-\theta)\sin\theta]/(1-\pi^2/4)$. Such an analytical solution is enforced at $x = 360$, $z = 360$, and $y = \pm 360$, as in Romanò et al. [48].

Owing to the symmetries and the linearity of our creeping flow problem, the original problem can be solved as superposition of four cases (one of which with two variants):

I) rotation of a sphere with axis parallel to the edge of a steady right corner:

$$\boldsymbol{U}_\mathrm{w} = \boldsymbol{0}, \quad \boldsymbol{U} = \boldsymbol{0}, \quad \boldsymbol{\Omega} = \Omega_y \boldsymbol{e}_y, \quad \boldsymbol{g} = \boldsymbol{0}, \tag{4}$$

II) translation of a sphere normal to one of the walls of a steady right corner:

$$\text{a)} \quad \boldsymbol{U}_\mathrm{w} = \boldsymbol{0}, \quad \boldsymbol{U} = U\boldsymbol{e}_x, \quad \boldsymbol{\Omega} = \boldsymbol{0}, \quad \boldsymbol{g} = \boldsymbol{0}, \tag{5a}$$
$$\text{b)} \quad \boldsymbol{U}_\mathrm{w} = \boldsymbol{0}, \quad \boldsymbol{U} = W\boldsymbol{e}_z, \quad \boldsymbol{\Omega} = \boldsymbol{0}, \quad \boldsymbol{g} = \boldsymbol{0}, \tag{5b}$$

III) a sphere held steady near a right corner with one of its walls sliding towards the edge:

$$\boldsymbol{U}_\mathrm{w} = U_\mathrm{w}\boldsymbol{e}_x, \quad \boldsymbol{U} = \boldsymbol{0}, \quad \boldsymbol{\Omega} = \boldsymbol{0}, \quad \boldsymbol{g} = \boldsymbol{0}, \tag{6}$$

IV) a sphere held steady near a stationary right corner under the effect of buoyancy forces:

$$\boldsymbol{U}_\mathrm{w} = \boldsymbol{0}, \quad \boldsymbol{U} = \boldsymbol{0}, \quad \boldsymbol{\Omega} = \boldsymbol{0}, \quad \boldsymbol{g} = ga^3/\nu^2(0,\ 0,\ 1), \tag{7}$$

where the wall and particle velocities have been normalized by ν/a_p, the particle rotation rate by ν/a_p^2, and the gravity acceleration is made non-dimensional by scaling it with ν^2/a_p^3.

3. Dynamics of a spherical particle

As the flow between the spherical particle and the dihedral corner is Stokesian, the dynamics of the particle can be computed using the quasi-steady approximation. Hence, the sphere does not experience any acceleration and the resultant of all the forces, as well as of all the torques, exerted by the fluid on the particle must be null. Following Ref. [45], we can write the translational and rotational equilibria for the particle centroid formulating the equations in terms of force and torque coefficients $\boldsymbol{F} = (F_x, F_y, F_z)$ and $\boldsymbol{T} = (T_x, T_y, T_z)$, where the forces and torques have been scaled by the Stokes drag $6\pi\rho_\mathrm{f}\nu a_\mathrm{p} U$ and the couple $8\pi\rho_\mathrm{f}\nu a_\mathrm{p}^2 U$. Owing to the symmetries of the problem, $\boldsymbol{U} = (U, 0, W)$ and $\boldsymbol{\Omega} = (0, \Omega_y, 0)$ and the linear system governing the particle dynamics reads:

$$\underbrace{\begin{pmatrix} F_x^{IIa} & F_x^{IIb} & F_x^{I} \\ F_z^{IIa} & F_z^{IIb} & F_z^{I} \\ T_y^{IIa} & T_y^{IIb} & T_y^{I} \end{pmatrix}}_{:=\boldsymbol{M}} \cdot \begin{pmatrix} U \\ W \\ \Omega_y \end{pmatrix} = -\begin{pmatrix} U_\mathrm{w}F_x^{III} \\ U_\mathrm{w}F_z^{III} \\ U_\mathrm{w}T_y^{III} \end{pmatrix} + \begin{pmatrix} 0 \\ 2/9(1-\rho)Fr^{-2} \\ 0 \end{pmatrix}$$
$$= -(A_1 \ \ A_2 \ \ A_3)^\mathrm{T}. \tag{8}$$

where $\rho = \rho_\mathrm{p}/\rho_\mathrm{f}$ is the particle-to-fluid density ratio, $Fr = \nu/\sqrt{ga_\mathrm{p}^3}$ is the Froude number, $U_g = (2/9)(1-\rho)Fr^{-2} = 2(1-\rho)ga_\mathrm{p}^3/9\nu^2$ is the dimensionless settling velocity (with $U_g > 1$ if $\rho < 1$ and *vice versa*), and the superscript identify the respective sub-problem of Fig. 2 for the force and torque coefficients that only depend on the position $\boldsymbol{x}_\mathrm{p}$ of the particle.

The solutions of Eq. (8) can be derived explicitly computing the translational and rotational velocity of the particle as done by Ref. [45], i.e., assuming that the fit functions of Ref. [48] hold:

$$\begin{pmatrix} U \\ W \\ \Omega_y \end{pmatrix} = \alpha_1 \begin{pmatrix} F_z^I T_y^{IIb} - F_z^{IIb} T_y^I \\ F_z^{IIa} T_y^I - F_z^I T_y^{IIa} \\ F_z^{IIb} T_y^{IIa} - F_z^{IIa} T_y^{IIb} \end{pmatrix} + \alpha_2 \begin{pmatrix} F_x^{IIb} T_y^I - F_x^I T_y^{IIb} \\ F_x^I T_y^{IIa} - F_x^{IIa} T_y^I \\ F_x^{IIa} T_y^{IIb} - F_x^{IIb} T_y^{IIa} \end{pmatrix}$$
$$+ \alpha_3 \begin{pmatrix} F_x^I F_z^{IIb} - F_x^{IIb} F_z^I \\ F_x^{IIa} F_z^I - F_x^I F_z^{IIa} \\ F_x^{IIb} F_z^{IIa} - F_x^{IIa} F_z^{IIb} \end{pmatrix}, \tag{9}$$

where $\alpha_i = A_i/\det(\boldsymbol{M})$.

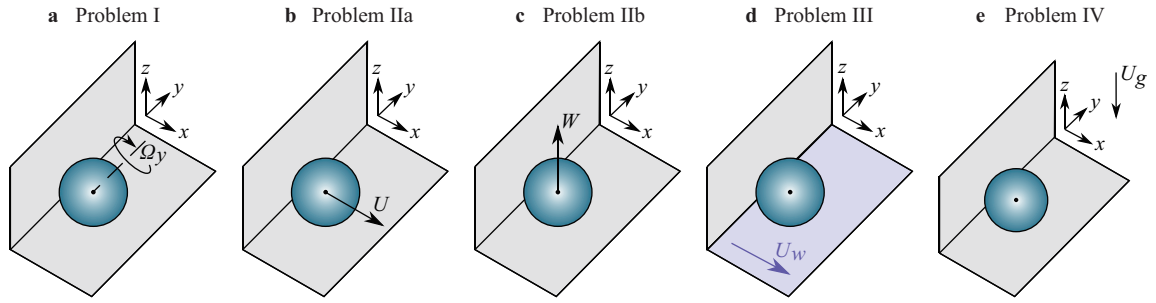

Figure 2 Decomposition of the general problem into elementary sub-problems. The arrows in **a**, **b** and **c** show the rotational and translational motion of the particle, the arrow in **d** denotes the sliding direction of the moving wall, while the arrow in **e** refers to the non-dimensional settling velocity U_g.

4. Phase space reconstruction

A meshless interpolant will be employed to numerically reconstruct the phase space of the particle dynamics. Following Ref. [46], we carry out a multiquadratic radial basis interpolation with radial basis functions $\phi(r)$ and scalar radius $r = \|\boldsymbol{r} - \boldsymbol{r}_i\|_2$ measured from the i-th generalized coordinate of the phase space, $\boldsymbol{r}_i$. Our multivariate function $f(\boldsymbol{r})$ to interpolate is each particle flow component in the $(x,\ z)$-plane, i.e., U and W. As they depend on the location of the particle centroid $\boldsymbol{x}$, on the wall velocity U_w, and on the characteristic settling velocity U_g, the generalized phase space coordinates are $\boldsymbol{r} = (x,\ z,\ U_\mathrm{w},\ U_g)$, and the basis function interpolant $f_\mathrm{RBF}(\boldsymbol{r}) \approx f(\boldsymbol{r})$ yields

$$f_\mathrm{RBF}(\boldsymbol{r}) = \sum_{l=1}^{L} \beta_l p_l(\boldsymbol{r}) + \sum_{n=1}^{N} \lambda_n \phi(\|\boldsymbol{r} - \boldsymbol{r}_n\|_2), \tag{10}$$

where N denotes the amount of nodes to interpolate, p_l are the elements of a hierarchical polynomial functional basis made use of for conditioning the interpolant f_RBF to be positive definite, and $L = 2$ is here used as the maximum polynomial order. For more details about the choice and optimization of all the remaining coefficients, we refer to Ref. [46].

5. Results and discussion

As recently demonstrated by Romanò et al. [45], the particle dynamics near a corner flow results from a dissipative system that admits a non-trivial attractor in $(x, z) \in [1.1,\ 2] \times [1.1,\ 2]$ for $U_g \in [-1.6,\ -0.7]$, if U_g is aligned with the z-direction as in our case. This is demonstrated in Fig. 3 for $U_\mathrm{w} = -1$, and $U_g = -1$ (Fig. 3a) and $U_g = -1.5$ (Fig. 3b). The blue lines denote the particle trajectories converging to the attractor (pink bullet). Owing to the linearity of the creeping flow solution, an equivalent repeller would emerge if we considered sign-inverted driving effects, i.e., for $U_\mathrm{w} = 1$ and $U_g = \{1,\ 1.5\}$.

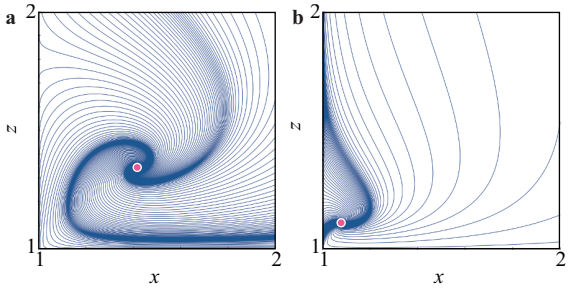

Figure 3 Particle attractor for $U_\mathrm{w} = -1$ and $U_g = -1$ **a** and $U_g = -1.5$ **b**. The blue lines denote the particle flow streamlines and the pink bullet show the location of the attractor.

The dynamics observed for the particle is dominated by gravitational and particle-boundary interaction effects. This is made clear by comparing Fig. 3a and b, which in turn are topologically different from the unperturbed flow streamlines (see light-blue square in Fig. 2). As a result, the strong sensitivity of the particle dynamics to the ratio between U_w and U_g renders very challenging to correct the particulate flow field for sedimentation effects. In fact, we will generalize the approach of Romanò [46] demonstrating that it can be used not only for the reconstruction of the unperturbed fluid flow, but also for robustly correcting the particulate flow field from sedimentation effects. We will therefore reconstruct the dynamics of neutrally buoyant particles ($U_g = 0$) in the whole domain by tracking only a few density mismatched particles.

To test our approach for reconstructing the flow of neutrally buoyant particles, we consider two tracking data sets, i.e., a few density-mismatched particle trajectories initialized: (i) at the same location $(x, z) = (2,\ 1.1)$, and (ii) along a vertical line at $x = 2$. Figure 4a depicts the particle trajectories corresponding to case (i) for $U_g \in [-2,\ 2]$ and $U_\mathrm{w} = -1$. The corresponding particle velocity $\boldsymbol{U} = (U,\ W)$, unperturbed flow velocity $\boldsymbol{u}_\mathrm{f} = (u_\mathrm{f},\ w_\mathrm{f})$ and particle-to-fluid velocity difference are depicted in Fig. 4b from right to left, respectively. The particle trajectories are sampled with a constant time step of $\Delta t = 0.01$ and integrated for $t = 150$ or until the particle leaves the domain $(x, z) = [1,\ 2] \times [1,\ 2]$. As we vary the characteristic settling velocity U_g, the particles init-

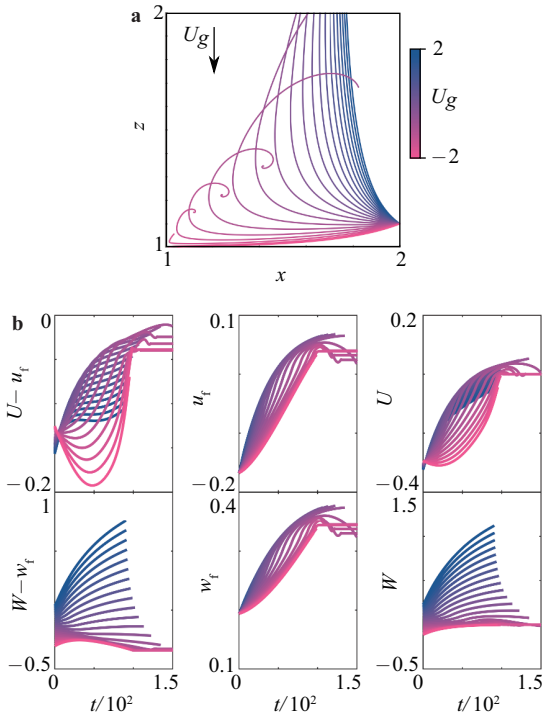

Figure 4 Trajectories **a** and velocities **b** for twenty-one particles with $U_g \in [-2,\ 2]$ and initialized at $(x, z) = (2,\ 1.1)$. The right panels denote the particle-to-unperturbed-fluid-flow velocity difference $(U - u_f, W - w_f)$, the unperturbed fluid velocity (u_f, w_f), and the particle velocity (U, W) as a function of time along the particle trajectory.

ialized at $(x, z) = (2,\ 1.1)$ gets attracted to a spiral sink, as shown for the lightest pink trajectories in Fig. 4a, while they exit the domain of interest for large enough U_g, i.e., $U_g > -0.7$. In the spirit of the approach developed by Romanò [46], different dissipative dynamics are combined by computing particle trajectories for various U_g/U_w. On the one hand, varying U_g/U_w allows to probe the domain by taking advantage of the spectrum of the dissipative systems considered; on the other hand, enlarging the absolute value of the control parameter $|U_g/U_w|$ leads to systems with a less pronounced spiralling character that either quickly converges to the spiral sink or quickly exits the domain of interest. We therefore decided to test the robustness of our approach by considering a limited subset of trajectories, $U_g = \{-0.8,\ -0.4,\ -0.2,\ -0.1,\ 0.1,\ 0.2,\ 0.4\}$, that include both the qualitative behaviours (attracted and domain-exiting trajectories) and that are used to correct the particulate flow for sedimentation effects. Figure 5a depicts the seven trajectories considered to sample the particle velocity $\boldsymbol{U}(x, z, U_w = -1, U_g)$ in the domain, and Fig. 5b shows the target flow to reconstruct computed using Eq. (9) for $U_g = 0$. The interpolation function (10) is used to reconstruct the particulate flow $\boldsymbol{U}$ in phase space $(x, z, U_w = -1, U_g)$, deriving the interpolant $\boldsymbol{U}_{RBF}(x, z, U_w = -1, U_g) = (U_{RBF}, W_{RBF})$. The robustness of the interpolant is tested by undersampling the original data set and computing the interpolation error. Comparing the interpolant reconstructed using a data sampling ratio of 0.5, 0.2, 0.1, and 0.05, a maximum relative error of less than 1% is found for the particle velocity probed along the trajectories shown in Fig. 4. Taking the limit for $U_g \to 0$ of the interpolated particle velocity in the hyperspace $(x, z, U_w = -1, U_g)$, an approximation of the flow field for neutrally buoyant particles $\hat{\boldsymbol{U}}(x, z, U_w = -1, U_g = 0)$ is derived over the whole domain, i.e., $\hat{\boldsymbol{U}}(x, z, U_w = -1, U_g = 0) = \lim_{U_g \to 0} \boldsymbol{U}_{RBF} \approx \boldsymbol{U}(x, z, U_w = -1, U_g = 0)$. A comparison between $\hat{\boldsymbol{U}}(x, z, U_w = -1, U_g = 0)$ and $\boldsymbol{U}(x, z, U_w = -1, U_g = 0)$ is depicted in Fig. 5c, where the former is depicted by pink arrows, while the latter is shown by green arrows. The good agreement between the original flow velocity for neutrally-buoyant particles and the reconstructed one is quantified by the absolute value of the error $|(\boldsymbol{U} - \hat{\boldsymbol{U}})_{U_g=0}|$ shown by the color map.

The second benchmark for the flow reconstruction approach proposed in this study considers particle trajectories initialized along $x = 2$ and shifted one another along the z-direction, i.e., $z = 1.1 + 0.2 \times (U_g + 2)$ for $U_g \in [-2,\ 2]$. The same values of $U_w = -1$ and U_g depicted in Fig. 4 are shown for this second test, and the corresponding particle orbits, velocities and unperturbed flow velocities are depicted in Fig. 6 with the same color coding and panels layout used for Fig. 4. This second benchmark is even more challenging than the first one as most of the particle trajectories considered do not

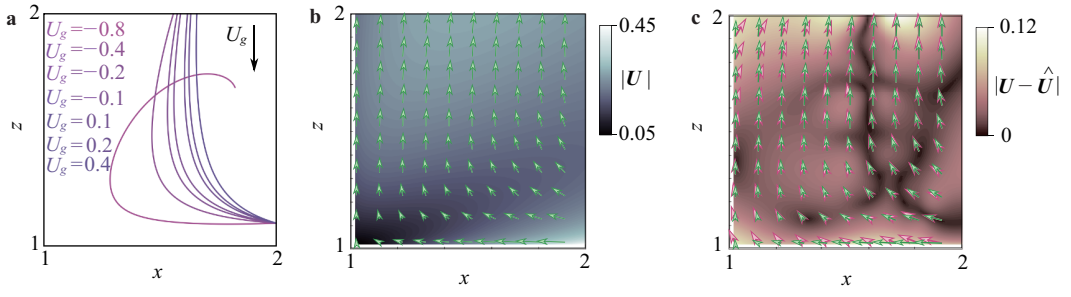

Figure 5 Set of particle trajectories selected for reconstructing the neutrally-buoyant particulate flow **a**, particle velocity field for $U_g = 0$ **b**, and reconstructed flow absolute error **c**. The green arrows show the target flow and the pink arrows denote the reconstructed particle flow.

provide any information about the flow near the vertical and horizontal walls. We however restrict even further the data set employed for demonstrating the robustness of our reconstruction algorithm by selecting only the trajectories for $U_g = \{-0.8, -0.4, -0.3, -0.2, -0.1, 0.1, 0.2, 0.3, 0.4\}$. We stress that the corresponding flow reconstruction over the whole target domain, i.e., for $(x, z) \in [1, 2] \times [1, 2]$, will mainly rely on a bundle of trajectories located at $x \in [\approx 1.9, 2]$ and $z \in [\approx 1.5, 2]$ (see Fig. 7a). The target particulate flow to reconstruct (Fig. 7b) is the same as in the first benchmark (Fig. 5b). Despite the increased difficulty, the flow reconstruction (pink arrows in Fig. 7c) keeps being in good agreement with the target flow (green arrows in Fig. 7c) as also quantified by the reconstruction error map $|(\boldsymbol{U} - \hat{\boldsymbol{U}})_{U_g=0}|$ shown in the background of Fig. 7c. In spite of the challenges of the two benchmarks, the reconstruction error is kept below 0.06 for most of the two-dimensional domain. The highest absolute error is localized near the bottom and left boundaries where the forces exerted by the wall on the particle tend to infinite, naturally ill-conditioning whatever form of reconstruction. We further stress that classic extrapolation algorithms applied for reconstructing the neutrally-buoyant dynamics are associated to a very significant absolute error, more than double in comparison to our method (not shown).

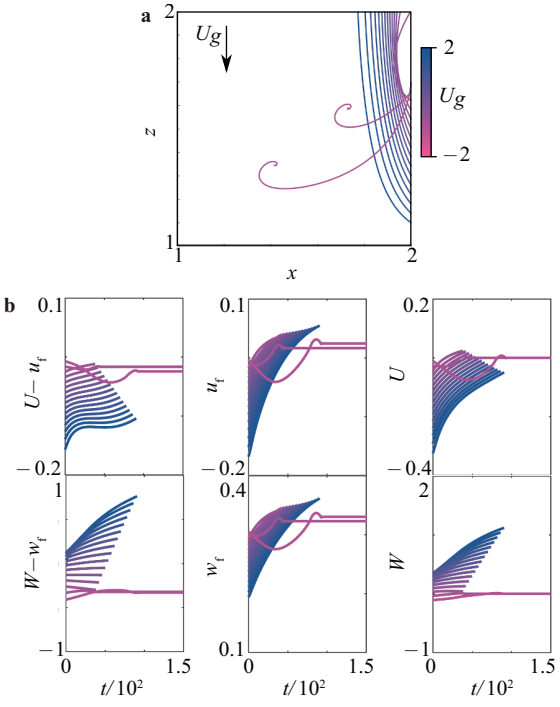

Figure 6 Trajectories **a** and velocities **b** for twenty-one particles with $U_g \in [-2, 2]$ and initialized at $(x, z) = (2, 1.1 + 0.2 \times (U_g + 2))$. The right panels denote the particle-to-unperturbed-fluid-flow velocity difference $(U - u_f, W - w_f)$, the unperturbed fluid velocity (u_f, w_f), and the particle velocity (U, W) as a function of time along the particle trajectory.

6. Summary and conclusion

The reconstruction of the velocity field for a neutrally-buoyant particle moving near a singular corner has been tackled by generalizing the approach firstly proposed by Romanò [46]. A few density-mismathed particle trajectories have been used to probe the flow field and the robustness of the algorithm has been demonstrated by considering two increasingly challenging benchmarks. At first, seven trajectories initialized from the same location have been considered. The orbits were relatively well-conditioned to probe a significant area of the near-corner flow, however, two qualitatively different dynamics have been included in this data set: (i) a particle getting attracted to a non-trivial spiralling sink, and (ii) six particles exiting the domain without any spiralling dynamics. Even if the quantitative and qualitative disagreement of the particle trajectories could ill-condition the reconstruction of the neutrally-buoyant particle flow $\boldsymbol{U}$ over the whole domain, our algorithm has been proven robust. This same satisfactory result has been obtained for the second test, in which a further element of ill-conditioning of the system has

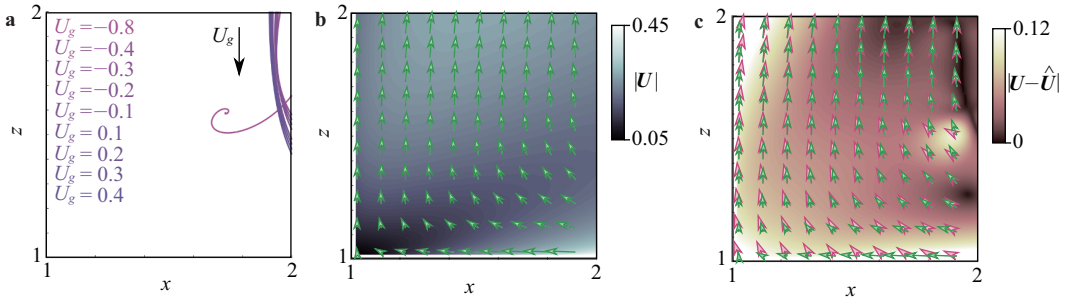

Figure 7 Set of particle trajectories selected for reconstructing the neutrally-buoyant particulate flow **a**, particle velocity field for $U_g = 0$ **b**, and reconstructed flow absolute error **c**. The green arrows show the target flow and the pink arrows denote the reconstructed particle flow.

been included. In fact, all the trajectories supposed to well condition the reconstruction operator have been gathered in a narrow bundle that could provide little information about the particles velocity in most of the domain. These two tests proved that the method proposed by Romanò [46] could well be adapted to correct for sedimentation effects by starting from the trajectory of density-mismatched particles and deriving the flow for a neutrally-buoyant particle all over the domain. Still, the largest errors of the reconstruction technique are distributed along the bottom and left edge of the particle centroid domain.

This consideration opens up to potential improvements of the reconstruction method that could take advantage of theoretical boundary conditions applied near each wall, as done for the background flow reconstruction [46]. The natural counterpart of the reconstructed flow for a neutrally-buoyant particle in Stokes flow is represented by the leading-order particle-boundary interaction dynamics predicted by the lubrication theory (see e.g., Refs. [16], [49] or [50]). Moreover, when the unperturbed flow reconstruction is aimed, the approach proposed in this study can well be used to correct for a dissipative effect at a time (sedimentation/density mismatch, particle-boundaries interaction, inertial effects) leading to the tracer equation. This same asymptotic limit can be approached from different directions either correcting for density mismatch at first and then for particle-boundaries interaction, or viceversa. That could help to approach the ultimate limit of inertia-less tracer particles and estimate the error committed by reconstructing the flow field.

The method proposed in this study is complementary to the classic theories of sedimentation [51, 52] and has potential applications to micron-sized centrifugation devices for particles in rotating cavity flows [53-57], to particle trapping/sorting [58-60], to particle attraction/repulsion in cavities [24, 61] and junction flows [62-65]. In general, within the framework of the creeping flow approximation and based on the definition of U_g, i.e., $U_g = 2(1-\rho)ga^3/9\nu^2$, the flow considered in this study applies to small particles suspended in liquids, i.e., $a \in [10^{-4},\ 10^{-3}]$ m and $\nu \in [10^{-6},\ 10^{-3}]$ m^2/s. For typical microfluidic flows, $a^3/\nu^2 \in [0.1,\ 10]$ s^2/m and our range of $U_g \in [-2,\ 2]$ leads to $|1-\rho| \in [0.1,\ 10]$.

1 W. C. Hinds, *Aerosol Technology: Properties, Behavior, and Measurement of Airborne Particles*, (John Wiley & Sons, Hoboken, 2012).
2 H. Burtscher, S. Künzel, and C. Hüglin, Characterization of particles in combustion engine exhaust, J. Aerosol Sci. **29**, 389 (1998).
3 A. R. Minerick, A. E. Ostafin, and H. Chang, Electrokinetic transport of red blood cells in microcapillaries, Electrophoresis **23**, 2165 (2002).
4 R. M. Iverson, M. E. Reid, and R. G. Lahusen, Debris-flow mobilization from landslides, Annu. Rev. Earth Planet. Sci. **25**, 85 (1997).
5 S. Razavi Bazaz, A. Mashhadian, A. Ehsani, S. C. Saha, T. Krüger, and M. Ebrahimi Warkiani, Computational inertial microfluidics: A review, Lab Chip **20**, 1023 (2020).
6 D. Jiang, C. Ni, W. Tang, D. Huang, and N. Xiang, Inertial microfluidics in contraction-expansion microchannels: A review, Biomicrofluidics **15**, 041501 (2021).
7 C. P. Moerland, L. J. van IJzendoorn, and M. W. J. Prins, Rotating magnetic particles for lab-on-chip applications—A comprehensive review, Lab Chip **19**, 919 (2019).
8 Z. Chen, L. Shen, X. Zhao, H. Chen, Y. Xiao, Y. Zhang, X. Yang, J. Zhang, J. Wei, and N. Hao, Acoustofluidic micromixers: From rational design to lab-on-a-chip applications, Appl. Mater. Today **26**, 101356 (2022).
9 M. J. Mitchell, M. M. Billingsley, R. M. Haley, M. E. Wechsler, N. A. Peppas, and R. Langer, Engineering precision nanoparticles for drug delivery, Nat. Rev. Drug Discov. **20**, 101 (2021).
10 F. Deeba, F. Umer, and D. Nainan, Applications of nanoparticles in treatment of respiratory disorders, Life and Science **3**, 8 (2021).
11 E. Ng, and V. Shah, Guidelines for surfactant replacement therapy in neonates, Paediat. Child Health **26**, 35 (2021).
12 T. P. Stevens, and R. A. Sinkin, Surfactant replacement therapy, Chest **131**, 1577 (2007).
13 M. R. Maxey, and J. J. Riley, Equation of motion for a small rigid sphere in a nonuniform flow, Phys. Fluids **26**, 883 (1983).
14 P. G. Saffman, The lift on a small sphere in a slow shear flow, J. Fluid Mech. **22**, 385 (1965).
15 A. J. Weisenborn, and B. I. M. ten Bosch, On the Oseen drag on a sphere, SIAM J. Appl. Math. **55**, 577 (1995).
16 H. Brenner, The slow motion of a sphere through a viscous fluid towards a plane surface, Chem. Eng. Sci. **16**, 242 (1961).
17 G. B. Jeffery, On the steady rotation of a solid of revolution in a viscous fluid, Proc. London Math. Soc. **s2_14**, 327 (1915).
18 F. Romanò, and H. C. Kuhlmann, Particle-boundary interaction in a shear-driven cavity flow, Theor. Comput. Fluid Dyn. **31**, 427 (2017).
19 W. P. Breugem, A second-order accurate immersed boundary method for fully resolved simulations of particle-laden flows, J. Comput. Phys. **231**, 4469 (2012).
20 A. J. Goldman, R. G. Cox, and H. Brenner, Slow viscous motion of a sphere parallel to a plane wall—II Couette flow, Chem. Eng. Sci. **22**, 653 (1967).
21 M. Chaoui, Creeping flow around a sphere in a shear flow close to a wall, Q. J. Mech. Appl. Math. **56**, 381 (2003).
22 J. Dauparas, and E. Lauga, Leading-order Stokes flows near a corner, IMA J. Appl. Math. **83**, 590 (2018).
23 M. M. Al-Hatmi and A. Purnama, On the motion of two microspheres in a stokes flow driven by an external oscillator field, Int. J. Math. Math. Sci. **2021** (2021)
24 F. Romanò, H. C. Kuhlmann, M. Ishimura, and I. Ueno, Limit cycles for the motion of finite-size particles in axisymmetric thermocapillary flows in liquid bridges, Phys. Fluids **29**, 093303 (2017).
25 J. Magnaudet, and M. Abbas, Near-wall forces on a neutrally buoyant spherical particle in an axisymmetric stagnation-point flow, J. Fluid Mech. **914**, A18 (2021).
26 F. Chowdhury, M. Ray, A. Passalacqua, P. Mehrani, and A. Sowinski, Evaluating the electrostatic charge transfer model for particle-particle interactions, J. Electrostatics **112**, 103603 (2021).
27 A. Babiano, J. H. E. Cartwright, O. Piro, and A. Provenzale, Dynamics of a small neutrally buoyant sphere in a fluid and targeting in Hamiltonian systems, Phys. Rev. Lett. **84**, 5764 (2000), arXiv: nlin/0007033.
28 M. Bouzaiene, M. Menna, D. Elhmaidi, A. F. Dilmahamod, and P. M. Poulain, Spreading of Lagrangian particles in the Black Sea: A comparison between drifters and a high-resolution ocean model, Remote Sens. **13**, 2603 (2021).
29 D. Schwabe, A. I. Mizev, M. Udhayasankar, and S. Tanaka, Formation of dynamic particle accumulation structures in oscillatory thermocapillary flow in liquid bridges, Phys. Fluids **19**, 072102 (2007).
30 F. Romanò, H. Wu, and H. C. Kuhlmann, A generic mechanism for finite-size coherent particle structures, Int. J. Multiphase Flow **111**, 42 (2019).
31 F. Romanò, and H. C. Kuhlmann, Finite-size Lagrangian coherent

structures in thermocapillary liquid bridges, Phys. Rev. Fluids **3**, 094302 (2018).
32 F. Romanò, Oscillatory switching centrifugation: Dynamics of a particle in a pulsating vortex, J. Fluid Mech. **857**, R3 (2018).
33 S. Xu, and A. Nadim, Oscillatory counter-centrifugation, Phys. Fluids **28**, 021302 (2016).
34 G. Haller, Lagrangian coherent structures, Annu. Rev. Fluid Mech. **47**, 137 (2015).
35 J. C. Lasheras, and K. K. Tio, Dynamics of a small spherical particle in steady two-dimensional vortex flows, Appl. Mech. Rev. **47**, S61 (1994).
36 N. Raju, and E. Meiburg, Dynamics of small, spherical particles in vortical and stagnation point flow fields, Phys. Fluids **9**, 299 (1997).
37 F. Romanò, and H. C. Kuhlmann, Numerical investigation of the interaction of a finite-size particle with a tangentially moving boundary, Int. J. Heat Fluid Flow **62**, 75 (2016).
38 B. Gereltbyamba, and C. Lee, Behavior of settling inertial particles in a differentially heated cubic cavity at moderate Rayleigh number, J. Mech. Sci. Technol. **32**, 3169 (2018).
39 F. Romanò, Particle coherent structures in confined oscillatory switching centrifugation, Crystals **11**, 183 (2021).
40 T. Sauma-Pérez, C. G. Johnson, L. Yang, and T. Mullin, An experimental study of the motion of a light sphere in a rotating viscous fluid, J. Fluid Mech. **847**, 119 (2018).
41 X. Ku, H. Li, J. Lin, and H. Jin, Accumulation of heavy particles in circular bounded vortex flows induced by two small rotating cylinders, Int. J. Multiphase Flow **113**, 71 (2019).
42 F. Romanò, P. Kunchi Kannan, and H. C. Kuhlmann, Finite-size Lagrangian coherent structures in a two-sided lid-driven cavity, Phys. Rev. Fluids **4**, 024302 (2019).
43 F. Romanò and H. C. Kuhlmann, Finite-size coherent structures in thermocapillary liquid bridges, Int. J. Micrograv. Sci. Appl. **36**, 360201 (2019)
44 H. Wu, F. Romanò, and H. C. Kuhlmann, Attractors for the motion of a finite-size particle in a two-sided lid-driven cavity, J. Fluid Mech. **906**, A4 (2021).
45 F. Romanò, P. E. des Boscs, and H. C. Kuhlmann, Stokesian motion of a spherical particle near a right corner made by tangentially moving walls, J. Fluid Mech. **927**, A41 (2021).
46 F. Romanò, Reconstructing the fluid flow by tracking of large particles, Phys. Rev. Fluids **4**, 104301 (2019).
47 G. I. Taylor, On scraping viscous fluid from a plane surface. In: Miszellaneen der Angewandten Mechanik (Festschrift Walter Tollmien) (M. Schäffer, ed.) (Akademie-Verlag, Berlin, 1962). pp. 313–315
48 F. Romanò, P. E. des Boscs, and H. C. Kuhlmann, Forces and torques on a sphere moving near a dihedral corner in creeping flow, Eur. J. Mech.-B Fluids **84**, 110 (2020).
49 H. Faxén, Z. Angew. Math. Mech. **7**, 79 (1927).
50 R. G. Cox, and H. Brenner, The slow motion of a sphere through a viscous fluid towards a plane surface－II Small gap widths, including inertial effects, Chem. Eng. Sci. **22**, 1753 (1967).
51 G. J. Kynch, A theory of sedimentation, Trans. Faraday Soc. **48**, 166 (1952).
52 J. W. Williams, K. E. Van Holde, R. L. Baldwin, and H. Fujita, The theory of sedimentation analysis, Chem. Rev. **58**, 715 (1958).
53 P. J. Mason, Forces on bodies moving transversely through a rotating fluid, J. Fluid Mech. **71**, 577 (1975).
54 D. Mark, S. Haeberle, G. Roth, F. von Stetten, and R. Zengerle, Microfluidic lab-on-a-chip platforms: Requirements, characteristics and applications, Chem. Soc. Rev. **39**, 1153 (2010).
55 J. Ducrée, S. Haeberle, S. Lutz, S. Pausch, F. Stetten, and R. Zengerle, The centrifugal microfluidic Bio-Disk platform, J. Micromech. Microeng. **17**, S103 (2007).
56 F. Candelier, Time-dependent force acting on a particle moving arbitrarily in a rotating flow, at small Reynolds and Taylor numbers, J. Fluid Mech. **608**, 319 (2008).
57 J. J. Bluemink, D. Lohse, A. Prosperetti, and L. van Wijngaarden, A sphere in a uniformly rotating or shearing flow, J. Fluid Mech. **600**, 201 (2008).
58 J. Nilsson, M. Evander, B. Hammarström, and T. Laurell, Review of cell and particle trapping in microfluidic systems, Anal. Chim. Acta **649**, 141 (2009).
59 M. Tanyeri, M. Ranka, N. Sittipolkul, and C. M. Schroeder, A microfluidic-based hydrodynamic trap: Design and implementation, Lab Chip **11**, 1786 (2011).
60 A. Karimi, S. Yazdi, and A. M. Ardekani, Hydrodynamic mechanisms of cell and particle trapping in microfluidics, Biomicrofluidics **7**, 021501 (2013).
61 S. J. Tsorng, H. Capart, D. C. Lo, J. S. Lai, and D. L. Young, Behaviour of macroscopic rigid spheres in lid-driven cavity flow, Int. J. Multiphase Flow **34**, 76 (2008).
62 S. T. Chan, S. J. Haward, and A. Q. Shen, Microscopic investigation of vortex breakdown in a dividing T-junction flow, Phys. Rev. Fluids **3**, 072201 (2018), arXiv: 1806.10754.
63 S. C. Hur, A. J. Mach, and D. Di Carlo, High-throughput size-based rare cell enrichment using microscale vortices, Biomicrofluidics **5**, 022206 (2011).
64 E. Sollier, D. E. Go, J. Che, D. R. Gossett, S. O'Byrne, W. M. Weaver, N. Kummer, M. Rettig, J. Goldman, N. Nickols, S. McCloskey, R. P. Kulkarni, and D. Di Carlo, Size-selective collection of circulating tumor cells using Vortex technology, Lab Chip **14**, 63 (2014).
65 A. Volpe, P. Paiè, A. Ancona, R. Osellame, P. M. Lugarà, and G. Pascazio, A computational approach to the characterization of a microfluidic device for continuous size-based inertial sorting, J. Phys. D-Appl. Phys. **50**, 255601 (2017).

中性悬浮粒子流在奇异角附近的重构

Francesco Romanò

摘要 在蠕动流动条件下, 针对靠近奇异角移动的颗粒进行悬浮效应修正. 一些密度不匹配的粒子轨迹被用来重建整个目标区域的中性悬浮粒子的动力学. 我们建议利用密度不匹配粒子的耗散动力学来探测目标区域. 然后, 通过重建密度不匹配颗粒流的相空间, 并将颗粒与流体密度比的极限值取为1, 检索整个区域的中性浮力颗粒流. 这种方法的鲁棒性通过对重建算子的目标函数实行有目的抖动(ill-conditioning)来证明. 事实上, 我们证明即使是依赖于质量不同、密度不匹配的轨道拓扑, 或者依赖于密集的轨道束, 而不是均匀分布的轨道, 我们的算法也能很好地执行. 最后讨论了该算法在微流体领域的潜在应用和改进.